RSC Advances

COMMUNICATION

View Article Online
View Journal | View Issue

Cite this: *RSC Adv.*, 2015, **5**, 20346

Received 20th November 2014
Accepted 3rd February 2015

DOI: 10.1039/c4ra14945a

www.rsc.org/advances

A selenium@polypyrrole hollow sphere cathode for rechargeable lithium batteries†

Jing Guo, Zhaoyin Wen,* Guoqiang Ma, Jun Jin, Weiqi Wang and Yu Liu

A selenium@polypyrrole hollow sphere composite cathode delivers a reversible specific discharge capacity of 400 mA h g^{-1} after 80 cycles and a 60% reduction in impedance of the cycled cells is obtained. The soluble polyselenide species are demonstrated to be confined by PPy hollow spheres, thus inhibiting the shuttle effect to a large extent.

Introduction

Rechargeable lithium batteries have always been attached great importance on account of the rapid progress of portable electronics and electric vehicles as well as their exploitation in wind and solar renewable energy.[1] The desire for rechargeable batteries with high energy densities, high efficiencies and good safety has been accelerating the development of new energy storage systems.[2] Other than those electrodes or systems based on conventional intercalation chemistry, Li–S[3–6] and Li–O_2 (ref. 7–9) batteries, which possess incredibly high theoretical energy densities and are of low cost, have caught significant attention from relevant researchers. However, the cycling performance of Li–O_2 cells is restricted by the large polarization and instability of electrolytes.[10] Li–S batteries suffer from the shuttle effect, where polysulfides, the intermediate discharge products, dissolve in the electrolytes and migrate to the lithium anode, leading to rather poor cyclability. In addition, the sulfur cathode is both an electronic and ionic insulator, which also limits the practical applications of Li–S batteries.[3] Therefore, the synthesis of new electrode materials and the study of their performance are indispensable in the development of lithium batteries.

Selenium, belonging to the same group as sulfur, with a high specific theoretical capacity of 675 mA h g^{-1} or 3253 mA h cm^{-3}, was first demonstrated as a candidate cathode material for lithium and sodium rechargeable batteries by Abouimrane *et al.*[11] They investigated the structural mechanisms for Li insertion in selenium-based electrodes and their results show that the trigonal structural Se finally transforms into an antifluorite-type Li_2Se phase during discharge. They also found that the redox shuttle effect in the Se cathode was less severe than that in a S cathode. Li–Se batteries are supposed to possess a large volumetric energy density, which is of greater importance than gravimetric energy density in terms of the low weight and portability of batteries. Moreover, selenium exhibits a quite high intrinsic electronic conductivity (1×10^{-3} S m^{-1}) that is about 20 orders of magnitude greater than that of sulfur,[11,12] indicating better electrochemical activity and better rate capability. Nevertheless, the shuttle effect in the Li–Se system that deteriorates the cycle performance due to the dissolution of polyselenide species in electrolytes remains a problem.[13] Some of the strategies used to address the similar issue in Li–S batteries can be applied to Li–Se batteries, such as carbon coating,[14–16] use of microstructures with various morphologies,[17,18] exploration of appropriate electrolyte systems[19–21] and other methods of modification.[22] Zhang *et al.* presented a simple way to improve the specific capacity of Li–Se batteries by inserting a conductive, porous carbon interlayer between the cathode and the separator.[23] Wu *et al.* prepared a Se–C cathode *via* low temperature treatment that delivered a capacity of 187 mA h g^{-1}, even at a current density of 500 mA g^{-1}.[24]

Conductive polymer compounds have been repeatedly used in Li secondary batteries due to their good electrochemical activities and better accommodation of volume expansion than carbon.[25] Polypyrrole was reported to be beneficial in improving the performance of Li–S batteries[26–28] and was also adopted for the Se cathode. Kundu *et al.*[29] studied the performance of nanofibrous selenium (20–50 nm) with a polypyrrole coating, synthesized by a surfactant-free solution method, as a cathode material and demonstrated that polypyrrole wrapping enhanced the capacity by withstanding the large magnitude of shrinkage and expansion in volume. Considering that polypyrrole has both electronic and ionic conductivity, which can

CAS Key Laboratory of Materials for Energy Conversion, Shanghai Institute of Ceramics, Chinese Academy of Sciences, Shanghai 200050, P. R. China. E-mail: zywen@mail.sic.ac.cn; Fax: +86-21-52413903; Tel: +86-21-52411704

† Electronic supplementary information (ESI) available. See DOI: 10.1039/c4ra14945a

diminish electrochemical polarization, we employed polypyrrole hollow spheres in the cathode for a Li–Se battery system in order to confine Se and polyselenides. The loss of active material and capacity fading were effectively suppressed.

Experimental

Synthesis of Se@PPy hollow sphere composite

PPy hollow spheres were synthesized using a modified template process as described in our previous work.[30] The Se@PPy hollow sphere composite was prepared using a melt-diffusion approach. A mixture of Se and PPy hollow spheres (PPy HS) with a 6 : 4 weight ratio was mixed uniformly by grinding for 30 minutes. Then the mixture was sealed in an evacuated glass tube and heated at 250 °C for 12 h. After that the composite was washed with CS_2 solvent 3 times to remove the unconfined Se.

Physical characterization

Field emission scanning electron microscopy (FESEM) images were obtained using a JSM-6700 field emission scanning electron microscope. Transmission electron microscopy (TEM) analysis was performed on a JEOL JEM-2010 transmission electron microscope operated at 200 kV. Elemental mapping results were examined using energy dispersive spectroscopy (EDS) with a spectrometer attached to the JEOL JEM-2010 transmission electron microscope. X-ray powder diffraction (XRD) analysis of the as-obtained samples was carried out with a Rigaku Ultima IV with CuK_α radiation ($\lambda = 1.54056$ Å) operated at 40 kV and 200 mA. Raman spectroscopy measurements were conducted using a DXR Raman Microscope (Thermo Fisher) with an excitation wavelength of 532 nm. An elemental analyser (Vario EL III, Elementar Corp.) was applied to determine the content of Se in the composite. The specific surface area was measured using the Brunauer–Emmett–Teller (BET) method on a Micromeritics Tristar 3000.

The cycled Li anode samples for SEM measurements were prepared in an argon-filled glove box. The cells were disassembled after cycling and the cycled Li foils were washed with pure 1,2-dimethoxyethane (DME, anhydrous, Sigma) and then dried for 2 h. A special transfer system[31] was employed to transfer the cycled lithium samples from the glove box to a SEM system without exposing them to air.

Electrochemical characterization

The electrochemical performance of the Se@PPy HS composite was assessed using CR2025 type coin cells assembled in an argon-filled glove box with oxygen and water contents less than 1 ppm. To prepare the cathode, a slurry containing 80 wt% composite material, 10 wt% acetylene black, 5 wt% carboxyl methyl cellulose and 5 wt% styrene–butadiene rubber, dissolved in a proper amount of deionized water, was mixed by ball milling at 250 r min^{-1} for 6 h. For comparison, a slurry of pristine selenium was prepared in the same way. After that, the slurries were pasted onto Al foil. The electrodes were dried at 60 °C under vacuum for 12 h after the solvent was evaporated and then were cut into discs that were 14 mm in diameter. A solution of 1 M lithium bis(trifluoro-methanesulfonyl)imide (LiTFSI) and 0.1 M $LiNO_3$ dissolved in 1,3-dioxolane (DOL)–DME with a volume ratio of 1 : 1 was employed as the electrolyte. A glass fiber disc and lithium foil were used as the separator and the anode, respectively.

Galvanostatic discharge/charge tests were performed on a LAND CT2001A battery test system (Wuhan, China) in a voltage range of 1.6–2.6 V (*vs.* Li/Li^+). AC impedance spectroscopy data were collected over a frequency range from 0.01 Hz to 1 MHz, with a potential amplitude of 10 mV, on an Autolab Electrochemical Workstation (ECO CHEMIE B.V, Netherlands). Cyclic voltammetry (CV) measurements were also conducted on the Autolab Electrochemical Workstation at 0.1 mV s^{-1} in the potential range of 1.0–3.0 V. All the electrochemical measurements were carried out at room temperature. The value of Coulombic efficiency is determined by dividing the discharge capacity by the charge capacity of each cycle.

Results and discussion

The morphology of the prepared PPy hollow spheres is shown in Fig. 1a and b. The hollow spheres are self-assembled from smaller polypyrrole particles, have an approximate diameter of 300 nm and present good shape and dispersibility, with nice uniformity not only in particle size but also in shell thickness. Fig. 1c shows the morphology of the Se@PPy HS composite and corresponding C and Se elemental mapping. With a high selenium content of 52.4 wt%, no distinct Se particles or agglomerations are observed around the PPy spheres. The EDS mapping results of the composite show a uniform distribution of Se within the spheres or on the outer surface of them, indicating the infiltration of selenium into the hollow spheres. Furthermore, the specific surface area of the composite dramatically decreases compared to that of PPy HS, as seen in Fig. S1,† which confirms the penetration of Se into PPy HS.

Fig. 2a shows the XRD patterns of pristine Se, PPy HS and the Se@PPy HS composite. All the diffraction peaks of pristine Se, of extreme sharpness and high intensity, can be indexed as

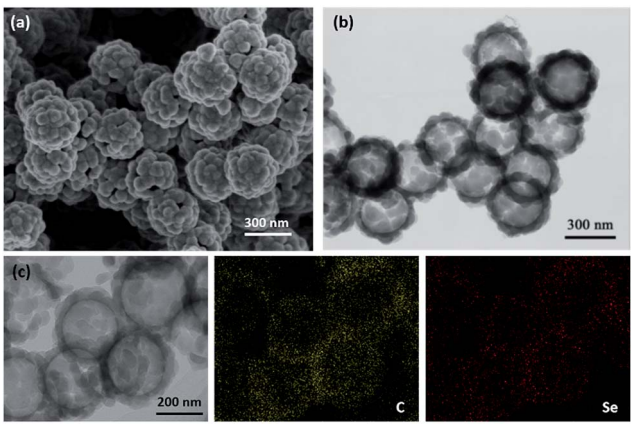

Fig. 1 (a) SEM image of PPy hollow spheres; (b) TEM images of PPy hollow spheres; (c) Se@PPy HS and corresponding C and Se elemental mapping.

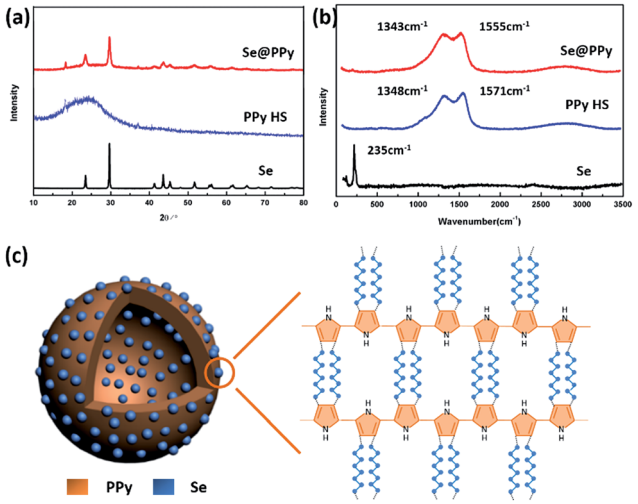

Fig. 2 (a) XRD patterns of Se, PPy HS and Se@PPy HS; (b) Raman spectra of Se, PPy HS and Se@PPy HS; (c) schematic illustration of the Se@PPy HS composite and a possible spatial structure for it.

those of the trigonal phase of selenium. By comparison, the identical diffraction peaks of Se in the Se@PPy HS composite become much weaker and broader, which indicates that some of the crystalline Se has become amorphous and most of the Se has diffused into the hollow spheres.

The structural features of the Se in the composite were further probed using Raman Spectroscopy (Fig. 2b). Compared with the pristine Se, the intensity of the characteristic peak of Se greatly decreases in the Se@PPy HS composite but the spectrum of the composite still shows a small peak at 236 cm^{-1} which corresponds to the chain-structured Se_n molecule,[32] thus indicating the impregnation of Se into the PPy hollow spheres.[13] Chain-like Se_n molecules are likely to exhibit superior electrochemical properties because of their strong interaction with the host matrix.[33] In the spectrum of PPy, a major broad band at 1348 cm^{-1} is assigned to a hybrid mode of intra-ring C–C bond stretching and mainly inter-ring C–C bond stretching, antisymmetrical C–N stretching, or ring stretching.[34] The other band at 1571 cm^{-1} is assigned to the C=C backbone stretch contributed by the cation species.[35] However, after encapsulation of Se into the PPy hollow spheres, the band at 1348 cm^{-1} red shifts to 1343 cm^{-1} while the C=C band shifts to 1555 cm^{-1}, which is attributed to neutral species.[35] The shift of bands reveals certain interactions between the Se and PPy matrix.

The schematic illustration of the Se@PPy HS composite and a possible spatial structure of it are shown in Fig. 2c. The thin wall of the PPy hollow sphere, which is favorable for both electron conduction and Li ion transport, can physically hinder the dissolution of polyselenides. The volume expansion during cycling can be well-buffered by the hollow space. Furthermore, the interaction force between chain-like Se_n and PPy generated during the heat treatment can also play a part in inhibiting the shuttle effect. According to the above Raman analysis, the C=C backbone stretch in PPy changes a little after the infiltration of Se. Therefore, we can speculate that part of the chain-like Se_n in the composite has certain interactions with the C atom in the C=C bonds, as indicated by the black dotted lines in Fig. 2c. Thus, a cross-linked Se–PPy network is developed. A similar phenomenon is observed in S@PPy composite.[30]

The CV curves of Li–Se and Li–Se@PPy HS cells are shown in Fig. 3. The curves of the pristine Se cathode vary a lot with the increase of scanning laps, while those of the Se@PPy HS cathode almost overlap, thus confirming that the composite cathode displays high reversibility and stability. The cathodic peak current of the composite electrode is 4 times higher than that of pristine Se, implying higher electrochemical activity of the Se@PPy HS cathode. During the initial discharge process of the Li–Se@PPy HS cell, two cathodic peaks at 2.04 V and 1.60 V are noted, corresponding to the conversion of elemental Se to polyselenides, and polyselenides to Li_2Se, respectively. Only one anodic peak (Li-extraction) is observed at 2.37 V in the subsequent anodic sweep to 3.0 V. In the second and third cycles, the reduction peaks shift by 0.03 V to a higher potential while the oxidation peaks shift to a lower potential by 0.04 V. The slight shift in the peak potentials indicates a decrease in electrochemical polarization and the good reversibility of the Se@PPy HS composite. Furthermore, the oxidation peak current becomes greater as the scanning continues, which is related to the activation of the electrochemical process.

Fig. 4a displays the galvanostatic discharge/charge voltage profiles of the Se@PPy HS cathode at 0.2 C between 1.6 V and 2.6 V. Consistent with the cyclic voltammetry curves, two discharge plateaus are shown in the discharge curves, which can be attributed to the two classical step reactions of elemental selenium with lithium during the discharge process.[36] The composite cathode delivers an initial discharge capacity of 630 mA h g^{-1}. Fig. 4b compares the specific discharge capacity and Coulombic efficiency of Se@PPy HS and pristine Se at a rate of 0.2 C. The pristine Se cathode presents rather poor cycling stability with a low reversible capacity of less than 45 mA h g^{-1} after 80 cycles. The severe capacity fading is ascribed to the shuttle effect with dissolution of polyselenide species generated during the discharging process, which also results in a lower Coulombic efficiency. By contrast, a specific discharge capacity of 400 mA h g^{-1} is obtained for the Se@PPy HS electrode after 80 cycles. Moreover, the Coulombic efficiency almost reaches 100%, indicating that the shuttle effect is effectively inhibited by the hollow structure of PPy matrix (the Coulombic efficiency displayed over a smaller scale range is shown in Fig. S2†). The large capacity loss during the first five cycles can be interpreted

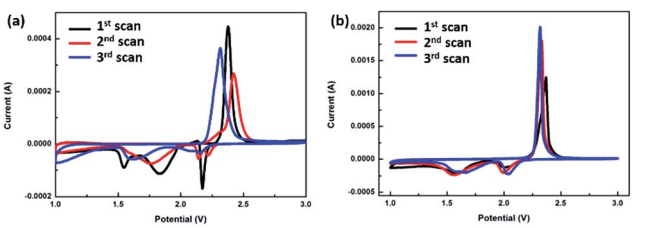

Fig. 3 Cyclovoltammetric behavior of pristine Se (a) and Se@PPy HS electrode (b) performed at a scan rate of 0.1 mV s^{-1} between 1.0 and 3.0 V against Li^+/Li.

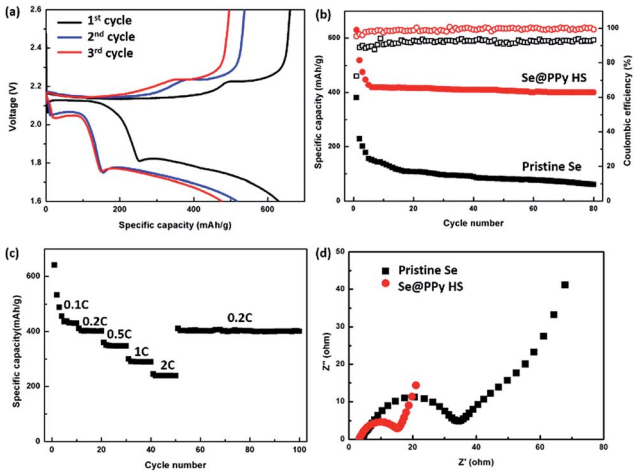

Fig. 4 (a) Galvanostatic discharge/charge voltage profiles of Se@PPy HS at 0.2 C; (b) cycling performance and Coulombic efficiency of Se@PPy HS and pristine Se at 0.2 C; (c) rate capability of Se@PPy HS cathode; (d) Nyquist plots of Li–Se@PPy HS and Li–Se cells after 50 cycles.

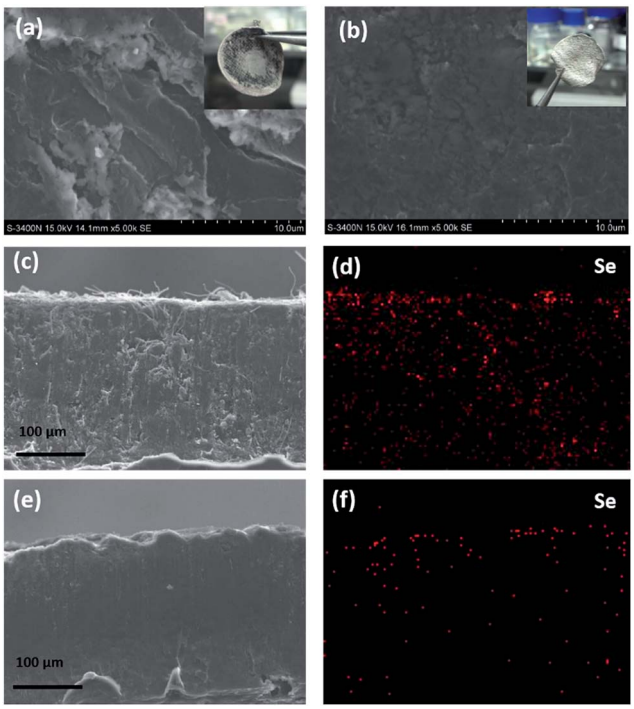

Fig. 5 SEM images of Li surfaces disassembled from the Li–pristine Se cell (a) and the Li–Se@PPy HS cell (b) after 50 cycles at 0.1 C (inset: pictures of corresponding Li anodes). SEM images and corresponding Se elemental mapping of Li cross-section disassembled from the Li–pristine Se cell (c and d) and the Li–Se@PPy HS cell (e and f) after 50 cycles at 0.1 C.

as follows. Some of the Se in the composite cathode is free and dissociative instead of being restricted inside the hollow spheres or connected with PPy. The polyselenide species generated by this dissociative Se during the discharge process dissolve in the electrolyte and migrate to the anode, thus resulting in the loss of active mass. It is the rest of the Se inside the hollow spheres or interacting with PPy that contributes to the stable discharge capacity in subsequent cycles.

The Se@PPy HS cathode also shows an excellent rate capability (Fig. 4c). The discharge capacity gradually decreases as the current rate increases from 0.1 C to 2 C (1 C is 675 mA h g^{-1}). A capacity of 238 mA h g^{-1} is retained at 2 C and it recovers to 402 mA h g^{-1} when the current rate is reduced back to 0.1 C, indicating the high reversibility of the composite cathode. Even after 100 cycles, a capacity of 399 mA h g^{-1} is retained. The good rate capability of the composite cathode can be attributed to the facile electronic/ionic transport and fast reaction kinetics in Se@PPy HS.

Electrochemical impedance spectroscopy (EIS) provides further evidence for the superior cyclability of the Se@PPy HS composite, as Fig. 4d indicates. The data show that the charge transfer resistance (R_{ct}) obviously decreases when pristine Se is substituted by Se@PPy HS as the cathode, demonstrating higher electrochemical activity of the composite cathode. The improved electrochemical activity can be ascribed to the reduced corrosion of the Li surface, which results from the suppression of shuttle effect during cycling.

After 50 cycles, the two kinds of cells were disassembled. The Li anodes were observed using photography on the macroscopic scale, as shown in the insets of Fig. 5. The displayed Li surface is the side close to the separator. It can be clearly seen that the Li anode from the Li–Se cell appears partially black and dark on the surface, indicating severe corrosion by the reaction with polyselenides. On the contrary, the cycled Li anode from the Li–Se@PPy HS cell presents a metallic lustre with little distinction from the fresh Li foil. The Li surface was further observed from the micro perspective. The Li anode from the Li–Se cell shows an uneven and coarse morphology (Fig. 5a) while a smooth and flat surface is shown in Fig. 5b, demonstrating that only a small amount of polyselenide migrates from the Se@PPy HS cathode to the anode side and thus the shuttle effect is greatly restrained.

The SEM images of the cycled Li cross-section provide further strong evidence for the shuttle effect suppression of the Se@PPy HS cathode. The corrosion of the Li anode by polyselenides in the Li–Se cell is so severe that both the upper surface and the internal mass are eroded as presented in Fig. 5c and d. By comparison, the cross-section of Li in the cycled Li–Se@PPy HS cell shows a little bit of corrosion (Fig. 5e and f). These results convincingly prove that the Se@PPy HS cathode successfully inhibits the shuttle effect and improves the electrochemical performance of the Li–Se battery by accommodating the soluble polyselenides into the hollow spheres and adsorbing them *via* certain interactions by PPy.

Conclusions

In summary, the Se@PPy HS composite, which delivers a specific discharge capacity of 400 mA h g^{-1} after 80 cycles and a Coulombic efficiency of nearly 100%, can be considered as a favorable cathode in a Li–Se battery system. Since the hollow sphere structure plays an effective role in accommodating and

confining soluble intermediate discharge products, the shuttle effect that brings about severe capacity fading and poor cycle performance is greatly suppressed.

Acknowledgements

The authors greatly acknowledge Prof. B. V. R. Chowdari (National University of Singapore) for his helpful discussions and the Natural Science Foundation of China for its financial support (NSFC, Projects no. 51402330 and no. 51201177).

Notes and references

1 M. Wakihara, *Mater. Sci. Eng., R*, 2001, **33**, 109–134.
2 J. Vetter, P. Novak, M. R. Wagner, C. Veit, K. C. Moller, J. O. Besenhard, M. Winter, M. Wohlfahrt-Mehrens, C. Vogler and A. Hammouche, *J. Power Sources*, 2005, **147**, 269–281.
3 X. L. Ji and L. F. Nazar, *J. Mater. Chem.*, 2010, **20**, 9821–9826.
4 A. Manthiram, Y. Z. Fu and Y. S. Su, *Acc. Chem. Res.*, 2013, **46**, 1125–1134.
5 J. R. Akridge, Y. V. Mikhaylik and N. White, *Solid State Ionics*, 2004, **175**, 243–245.
6 P. G. Bruce, S. A. Freunberger, L. J. Hardwick and J. M. Tarascon, *Nat. Mater.*, 2012, **11**, 19–29.
7 Z. L. Wang, D. Xu, J. J. Xu, L. L. Zhang and X. B. Zhang, *Adv. Funct. Mater.*, 2012, **22**, 3699–3705.
8 R. Black, B. Adams and L. F. Nazar, *Adv. Energy Mater.*, 2012, **2**, 801–815.
9 Z. Q. Peng, S. A. Freunberger, Y. H. Chen and P. G. Bruce, *Science*, 2012, **337**, 563–566.
10 R. Padbury and X. W. Zhang, *J. Power Sources*, 2011, **196**, 4436–4444.
11 A. Abouimrane, D. Dambournet, K. W. Chapman, P. J. Chupas, W. Weng and K. Amine, *J. Am. Chem. Soc.*, 2012, **134**, 4505–4508.
12 L. Liu and Y. Wu, *Chem. Commun.*, 2013, **49**, 11515–11517.
13 C. P. Yang, S. Xin, Y. X. Yin, H. Ye, J. Zhang and Y. G. Guo, *Angew. Chem., Int. Ed.*, 2013, **52**, 8363–8367.
14 X. Liang, Z. Y. Wen, Y. Liu, H. Zhang, J. Jin, M. F. Wu and X. W. Wu, *J. Power Sources*, 2012, **206**, 409–413.
15 M. Q. Zhao, X. F. Liu, Q. Zhang, G. L. Tian, J. Q. Huang, W. C. Zhu and F. Wei, *ACS Nano*, 2012, **6**, 10759–10769.
16 F. Wu, J. Z. Chen, L. Li, T. Zhao and R. J. Chen, *J. Phys. Chem. C*, 2011, **115**, 24411–24417.
17 J. Y. Li, B. Ding, G. Y. Xu, L. R. Hou, X. G. Zhang and C. Z. Yuan, *Nanoscale*, 2013, **5**, 5743–5746.
18 X. A. Liang, Z. Y. Wen, Y. Liu, H. Zhang, L. Z. Huang and J. Jin, *J. Power Sources*, 2011, **196**, 3655–3658.
19 S. S. Jeong, Y. T. Lim, B. S. Jung and K. W. Kim, *Mater. Sci. Forum*, 2005, **486–487**, 594–597.
20 S. S. Zhang, *Electrochim. Acta*, 2013, **97**, 226–230.
21 S. Z. Xiong, K. Xie and X. B. Hong, *Chem. J. Chin. Univ.*, 2011, **32**, 2645–2649.
22 J. Q. Huang, Q. Zhang, S. M. Zhang, X. F. Liu, W. C. Zhu, W. Z. Qian and F. Wei, *Carbon*, 2013, **58**, 99–106.
23 Z. Zhang, Z. Zhang, K. Zhang, X. Yang and Q. Li, *RSC Adv.*, 2014, **4**, 15489.
24 L. Liu, Y. Hou, Y. Yang, M. Li, X. Wang and Y. Wu, *RSC Adv.*, 2014, **4**, 9086.
25 Y. Yang, G. Zheng and Y. Cui, *Chem. Soc. Rev.*, 2013, **42**, 3018–3032.
26 Y. Fu and A. Manthiram, *RSC Adv.*, 2012, **2**, 5927–5929.
27 Y. Zhang, Y. Zhao, D. The Nam Long, A. Konarov, D. Gosselink, H. G. Soboleski and P. Chen, *Solid State Ionics*, 2013, **238**, 30–35.
28 Y. Zhang, Y. Zhao, A. Konarov, D. Gosselink, Z. Li, M. Ghaznavi and P. Chen, *J. Nanopart. Res.*, 2013, **15**, 1–7.
29 D. Kundu, F. Krumeich and R. Nesper, *J. Power Sources*, 2013, **236**, 112–117.
30 G. Ma, Z. Wen, J. Jin, Y. Lu, X. Wu, C. Liu and C. Chen, *RSC Adv.*, 2014, **4**, 21612.
31 S. Xiong, K. Xie, Y. Diao and X. Hong, *Electrochim. Acta*, 2012, **83**, 78–86.
32 C. Luo, Y. H. Xu, Y. J. Zhu, Y. H. Liu, S. Y. Zheng, Y. Liu, A. Langrock and C. S. Wang, *ACS Nano*, 2013, **7**, 8003–8010.
33 H. Ye, Y.-X. Yin, S.-F. Zhang and Y.-G. Guo, *J. Mater. Chem. A*, 2014, **2**, 13293–13298.
34 V. Eshkenazi, E. Peled, L. Burstein and D. Golodnitsky, *Solid State Ionics*, 2004, **170**, 83–91.
35 K. Crowley and J. Cassidy, *J. Electroanal. Chem.*, 2003, **547**, 75–82.
36 Y. Cui, A. Abouimrane, J. Lu, T. Bolin, Y. Ren, W. Weng, C. Sun, V. A. Maroni, S. M. Heald and K. Amine, *J. Am. Chem. Soc.*, 2013, **135**, 8047–8056.

